



# HHS Public Access

## Author manuscript

*Anal Chem.* Author manuscript; available in PMC 2020 May 30.

Author Manuscript

Author Manuscript

Author Manuscript

Author Manuscript

Published in final edited form as:

*Anal Chem.* 2019 August 06; 91(15): 9813–9818. doi:10.1021/acs.analchem.9b01481.

## Building Dynamic Cellular Machineries in Droplet-Based Artificial Cells with Single-Droplet Tracking and Analysis

Meng Sun, Zhengda Li, Shiyuan Wang, Gembu Maryu, Qiong Yang\*

Department of Biophysics, University of Michigan, 930 N. University Avenue, Ann Arbor, Michigan 48109, United States

### Abstract

Although the application of droplet microfluidics has grown exponentially in chemistry and biology over the past decades, robust universal platforms for the routine generation and comprehensive analysis of droplet-based artificial cells are still rare. Here we report using microfluidic droplets to reproduce a variety of types of cellular machinery in *in vitro* artificial cells. In combination with a unique image-based analysis method, the system enables full automation in tracking single droplets with high accuracy, high throughput, and high sensitivity. These powerful performances allow broad applicability evident in three representative droplet-based analytical prototypes that we develop for (i) droplet digital detection, (ii) *in vitro* transcription and translation reactions, and (iii) spatiotemporal dynamics of cell-cycle oscillations. The capacities of this platform to generate, incubate, track, and analyze individual microdroplets via real-time, long-term imaging unleash its great potential in accelerating cell-free synthetic biology. Moreover, the wide scope covering from digital to analog to morphological detections makes this droplet analysis technique adaptable for many other divergent types of droplet-based chemical and biological assays.

### Graphical abstract

---

\*Corresponding Author qiongy@umich.edu.

#### ASSOCIATED CONTENT

##### Supporting Information

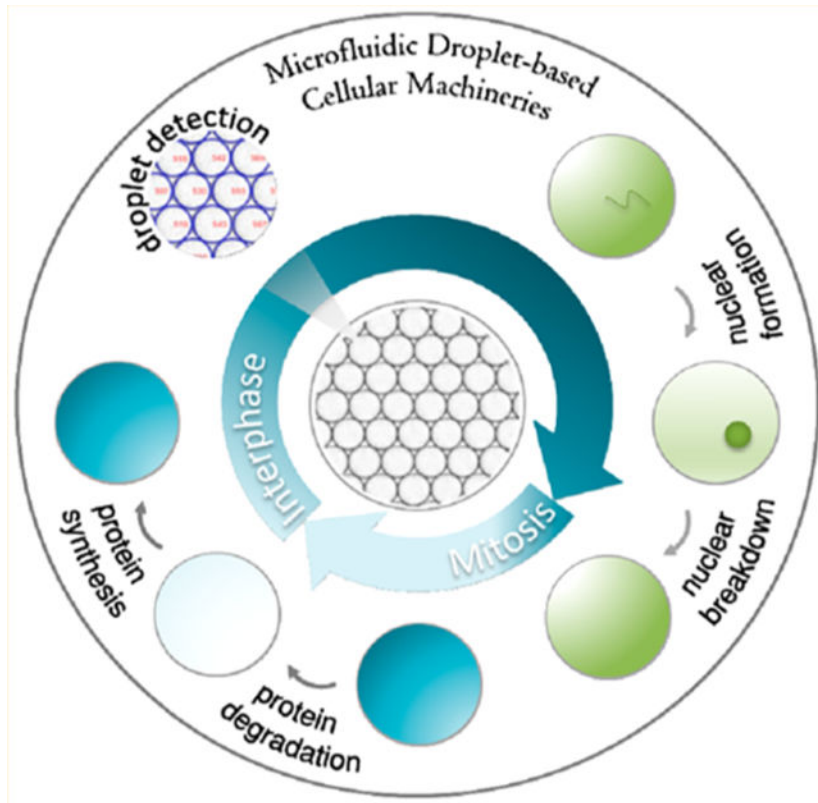
The Supporting Information is available free of charge on the ACS Publications website at DOI: [10.1021/acs.anal-chem.9b01481](https://doi.org/10.1021/acs.anal-chem.9b01481).

Figures and models showing details of droplet analysis, transcription and translation dynamics, mitotic and interphase discrimination and simulation (PDF)

Movie S1 showing droplet tracking (AVI)

Movie S2 showing nuclear formation and breakdown in cell cycle oscillations (AVI)

The authors declare no competing financial interest.



Synthetic biology has attracted increasing interests because of its ability to engineer artificial networks from the bottom up to mimic the behaviors of complex natural systems.<sup>1,2</sup> Compared to the *in vivo* synthetic biology approach, which relies on the living organism to host the synthetic pathway, the emerging and rapidly growing cell-free technologies enable the creation of *in vitro* artificial systems that contain only essential recombinant molecules and offer high flexibilities to tune stoichiometry and interactions of biological networks.<sup>3–5</sup> Such systems have been previously reconstructed in well-mixed bulk solutions, lacking the ability to imitate the hierarchical architecture achieved by functional cellular and subcellular compartmentalization, a key characteristic of a cell to maintain a certain size and keep the inner chemical contents separated from the outside environment. Studies have shown that compartmentalization is essential to modulate various cellular behaviors, such as cell divisions,<sup>6</sup> gene expression patterns,<sup>7</sup> scaling of intracellular structures,<sup>8,9</sup> and stochastic oscillations,<sup>10</sup> in a size-dependent manner. Therefore, to fully exploit the power of cell-free synthetic biology necessitates technical breakthroughs to create and analyze cell-scale and subcellular compartments.

Droplet microfluidic technology has emerged as one of the state-of-art technologies<sup>11–13</sup> that are capable of producing such cell-like compartments and subcompartments, as recently evidenced by the formations of a nucleus,<sup>14</sup> divisome,<sup>15</sup> microtubules,<sup>16</sup> and spindle<sup>8,9</sup> in uniform-sized droplets. By making monodispersed droplets from small sample volumes at high throughputs,<sup>17–21</sup> it allows expeditious processing of raw samples prepared from live embryos or cells that often times have unpredictable and limited quantities and thus can help

Author Manuscript  
Author Manuscript  
Author Manuscript  
Author Manuscript

maximally preserve the biological activities of the samples *in vitro*. These distinguished advantages in droplet production, however, pose high demands for the development of advanced droplet detection techniques with compatible analytical throughput and spatiotemporal resolution. In addition, for those artificial droplet cells that mimic cellular behaviors and biological processes, it becomes especially challenging to capture the sophisticated dynamics and morphological details in the droplets for long-term live monitoring. These challenges have consequently limited the technology to be generalizable to a broader range of applications.

Here we developed a droplet microfluidic toolbox (Figure 1A) and an image-based droplet analysis framework (Figure 1B) that address the aforementioned challenges to create and analyze artificial droplet cells. As shown in Figure 1B, droplets are generated in a flow-focusing device (i) and loaded from an on-chip reservoir into rectangular-shaped thin glass tubes (ii), which eliminate the need of space by microwells or microtraps fabricated on a chip and the complexity of manipulating fluid dynamics in microchannel network.<sup>22,23</sup> The tubes are then immersed and arrayed in an oil dish for long-term droplet incubation (iii) and imaging (iv). Unlike previously reported methods which apply additional fluorescence dyes to label droplets for segmentation and tracking,<sup>24,25</sup> which may be subject to cross-talk, photobleaching, fluctuations, and toxicity to biological samples, we developed an automatic image analysis method using bright-field images alone to segment and track every single droplet over the entire acquisition time (v). Fluorescence reporters were only introduced to report the dynamic processes of biological events. This is especially advantageous to biological assays that require multiple fluorescence reporters to record dynamic processes. We compare all droplets between two consecutive frames for the globally optimal matches (see Figure S2 and the Supporting Information for details)<sup>26</sup> to allow robust tracking. Each droplet is assigned with a unique ID, and its fluorescence intensity is measured and recorded frame by frame over all the captured time-lapse images.

Having the combinational advantages of high-throughput droplet generation and long-term incubation, as well as accurate tracking and detection, our droplet microfluidic framework can be flexibly adapted into a wide variety of chemical and biological applications. In the following, we demonstrate the powerful analytical capabilities of this system for three representative interrelated applications, that is, digital detection, analog kinetic measurement, and morphology characterization (Figure 1C). It will pave the way for quantitative characterization of biological circuits that are otherwise hard to access in bulk solutions or living organisms. To our best knowledge, no such comprehensive analytical capabilities in one set of tools have been reported to analyze droplet-based assays.

## EXPERIMENTAL SECTION

### Chemicals, Materials, and Instrument.

The 18.3 MΩ deionized water was used throughout the experiment. 2% 008-FluoroSurfactant in HFE7500 (Ran Biotechnologies, Inc., Beverly, MA) was used as the oil phase for microfluidics. The 1 μM fluorescein sodium and NHS-Rhodamine were prepared in water.

The oil and aqueous phases were driven with a dual-channel syringe pump (78–0388, KD Scientific, Holliston, MA). Microbore PTFE tubings (0.3 mm i.d., 0.76 mm o.d., Cole Parmer, Vernon Hills, IL) were used for fluidic connections. Glass tubes (inner dimension: 100  $\mu\text{m}$  in height, 2 mm in width, VitroCom, Mountain Lakes, NJ) were cut into 3–5 mm pieces using a ceramic scoring wafer (Restek, Bellefonte, PA) and then placed in a vacuumed desiccator with vaporized trichloro (1*H*,1*H*,2*H*,2*H*-perfluorooctyl)silane (Sigma-Aldrich, St. Louis, MO) for at least 1.5 h.

When droplets were generated and loaded into the glass tubes, the tubes were immersed in a glass-bottom Petri dish (Electron Microscopy Sciences, Hatfield, PA) filled with mineral oil (Macron Fine Chemicals, Avantor, Center Valley, PA) to prevent oil and sample evaporation. Images of droplets were then captured by a digital CMOS camera (ORCA-flash4.0 V3, Hamamatsu, Japan) installed on an inverted fluorescence microscope (IX83, Olympus, Japan), which was controlled by  $\mu$ Manager, an open source microscopy software (Vale Lab, UCSF, San Francisco, CA), for automatic stage positioning and droplet imaging. An experimental setup is shown in Figure S1. Control experiments were performed on a microplate reader (SpectraMax iD3, Molecular Devices, San Jose, CA) and the results shown in Figure S3.

### Fluorescence-Labeled Reporters.

GFP-NLS protein was prepared using a method described earlier.<sup>14</sup> Securin-CFP plasmids were constructed using the Gibson assembly method.<sup>27</sup> Securin-CFP mRNAs were in vitro transcribed and purified using mMESSAGE mMACHINE SP6 Transcription Kit (Ambion AM1340, Thermo Fisher Scientific, Waltham, MA).

### Cell-Free System Reconstruction.

In vitro transcription and translation (TXTL) and translation-only (TL) systems were constructed by mixing SP6 wheat germ extract (Promega, Madison, WI), securin-CFP plasmid DNA to a final concentration of 80 ng/ $\mu\text{L}$  (for TXTL), or securin-CFP recombinant mRNAs to a final concentration of 74 ng/ $\mu\text{L}$  (for TL), and complemented with water to a final volume of 25  $\mu\text{L}$ . Cycling *Xenopus* extracts were prepared as previously described,<sup>28</sup> except that eggs were activated with calcium ionophore A23187 (200 ng/ $\mu\text{L}$ ) rather than electric shock. Freshly prepared extracts were aliquoted into several 25  $\mu\text{L}$  volumes and mixed with demembranated sperm chromatin, GFP-NLS (10  $\mu\text{M}$ ), and energy mix.<sup>14</sup>

### Droplet Analysis.

Droplet-based image processing was performed using custom MATLAB (MathWorks, Natick, MA) scripts. Bright field images were used for segmentation and tracking of individual droplets. Segmentation was achieved by a watershed algorithm with seed generated from the Hough circle detection. Tracking was performed by maximizing the segmentation feature correlation between two consecutive time frames. Intensities from the fluorescent channels were calculated for each droplet track to obtain the fluorescence time traces. See the Supporting Information for detailed algorithms.

### Modeling and Fitting.

Both the transcription/translation model and the cell cycle model were adapted from previous publications.<sup>14,29–31</sup> All numerical simulations were performed using custom scripts written in MATLAB. For the transcription/translation model, parameters were fitted with experimental data using the Trust-region algorithm. See the Supporting Information for details.

### Device Fabrication.

An SU-8 mold on silica wafer was first fabricated to replicate PDMS slabs (~5 mm thick) with microfluidic channels (40  $\mu\text{m}$  in depth) via traditional photolithography and soft lithography methods.<sup>18</sup> Fluidic access holes and the droplet collection reservoir were then made by punching through the PDMS slabs using dispensing tips (0.7 mm, Jensen Global Inc., Santa Barbara, CA) and biopsy punches (4 mm, Integra LifeSciences Corporation, Plainsboro, NJ), respectively. In the last step, the thick slab was bonded to a thin and half-cured PDMS layer (~80  $\mu\text{m}$ ) spin coated on a glass slide, making the device ready for use after an additional 1 h bake in an oven at 70 °C.

## RESULTS AND DISCUSSION

### Digitalized Detection.

Analogous to the revolutionizing role of digital circuits in electronics, digital microfluidics offers a transformative potential in ultrasensitive molecular analyses at single-droplet and single-molecule levels. The concept has been most notably advanced by the droplet digital PCR (ddPCR) technique, where droplet detection has been most successfully achieved by incorporating inconvenient droplet reinjection into a second device with an extra pricey set of instruments for flow detection.<sup>32,33</sup>

Bearing the ultimate aims of analyzing droplet-based artificial cells, we first demonstrate the fundamental capabilities of our system for digital assays. We mixed two populations of water and fluorescent droplets in a tube. Time-lapse bright-field and fluorescence images were acquired in sequence at an interval of 3 min over a course of 5 h. Figure 2A shows an example image of droplets packed and assigned with an ID number in a  $2 \times 3 \text{ mm}^2$  area (seeing also the enlarged view in Figure 2B). Out of a total of 790 initially detected droplets, 770 (>97%) were tracked throughout the 5 h acquisition period. The lost droplets mostly resided at edges of the tube, either hiding in the shadows on the horizontal sides or escaping from the top or bottom opening of the tube (Movies S1). A total of 319 fluorescent droplets (Figure 2B, green circles G+) among the 770 were clearly distinguished from the rest of the 451 blank ones (Figure 2B, gray circles G-) by their relative intensities.

We further demonstrate this method can distinguish droplets with multiple fluorescent markers, which is useful for multichannel digital detections. Droplets of blank (G – R–), green only (G + R–), red only (G – R+), and green and red 1:1 mixture (G + R+), were randomly mixed and loaded in a tube and imaged. An enlarged view of a portion of droplets was shown in the bright field merged with fluorescent channels (Figure 2C). Four distinct

species of droplets can be clearly detected and sorted by their fluorescence colors and intensities (Figure 2D).

The capabilities of droplet indexing, tracking, measuring, sorting, and multiplexing make our system not just limited to droplet detections in binary and digital formats (i.e., 0 or 1 with assigned unique IDs) for end-point analysis; further, it can be of great usefulness for more advanced analytical applications that involve monitoring complex, long-term kinetic reconstitution, for example, in artificial droplet-cell assays, as we demonstrate in the following sections.

### In Vitro Transcription and Translation.

Protein synthesis and degradation are among the most essential reactions of a cell and can provide a fundamental source-sink basis for various complicated nonlinear dynamic processes (e.g., genetic switches, oscillations, morphogenesis, etc.). However, analyzing transcription and translation can be difficult in live cells since these processes are embedded in larger complex genetic regulatory networks that are subject to changes in intracellular and extracellular environments. Using cell-free extract, these processes can be isolated and better controlled, which directly led to the deciphering of RNA codons in the early 1960s.<sup>34</sup> Recent research has shown that cell-free expression system can also be used to engineer genetic circuits,<sup>35</sup> perform fast and scalable screens to characterize gene editing systems, such as CRISPR-Cas,<sup>36</sup> and, in combination with droplet microfluidics, produce a detailed dynamical analysis of transcription/ translation process.<sup>37,38</sup>

To demonstrate the analytical power of our system in kinetic measurements, we reconstituted cell-free TXTL and TL systems side by side, by encapsulating wheat germ extracts supplied with plasmid DNA (Figure 3A,B) and mRNAs (Figure 3C,D), respectively, of securin-CFP. Securin is a separase binding protein that prevents premature chromosome separation, which is critical for reliable cell cycle progression. In live cells, securin is actively synthesized in interphase and degraded upon anaphase onset, which makes it complicated to study its translation kinetics. This assay enabled high-resolution, high-throughput, real-time kinetic measurements of both TXTL and TL reactions simultaneously for more than 10 h.

Interestingly, in the TXTL system, which undergoes a two-step transcription and translation process, droplets show an increasingly larger variance in intensities over time compared to the TL-alone assay, as indicated by the higher heterogeneity in brightness of droplets (Figure 3A vs C) and the wider distribution of the curve intensity (Figure 3B vs D) after the transcription and translation initiated (Figure 3E). We attribute the more pronounced increasing variations of protein expression in the TXTL system to the additional transcription noise (i.e., stochastic mRNA production and degradation rates) in pL-scale encapsulations, compared to the TL system; it was found that such variation was not caused by the dispersed sizes of droplets (Figure S4). To further verify this hypothesis, we built a model (see the Supporting Information) based on previous research<sup>28,29</sup> to simulate the transcription and translation processes over time. By fitting each curve with our model, we found that the translation resource variation produces similar effects on both systems, while

the introduction of transcriptional resource variation among droplets in the TXTL system can account for their differential variations (Figure S5), supporting our hypothesis.

### Reconstitution of Cell Cycle Oscillations.

One of the ultimate goals of cell-free synthetic biology is to assemble an artificial cell from the bottom up to mimic the morphological and functional features of a biological cell.

However, most state-of-the-art engineering of the artificial cell has been limited to a mixed soup of molecules in a liposome-like structure. The behavior of these cells is far from the like of a real cell, failing to recapitulate the sophisticated out-of-equilibrium dynamics and spatial compartmentalization.

In the in vitro TXTL and TL systems, droplets eventually reach a stable equilibrium in securin protein expression (Figure 3B,D). In real cells that proliferate, a cell-cycle oscillator centered on cyclin-dependent kinase (Cdk1) and anaphase-promoting complex or cyclosome (APC/C) drives the alternations of synthesis and degradation of securin repeatedly, resulting in more complicated rhythmic dynamics (Figure 4A,B, “simple” cell). To demonstrate that our droplet system is amenable for reconstruction and analysis of cell-autonomous rhythmic dynamics that resembles real cells, we rebuild cell-cycling machinery using freshly prepared *Xenopus laevis* cytosolic egg extracts encapsulated in cell-sized droplets to create artificial cells. Incorporating securin-CFP mRNAs into the droplet system as a reporter, we observed that securin was synthesized during interphase (Figure 4C, rising phase) and degraded during anaphase (Figure 4C, falling phase) in a recurrent manner, indicating that these artificial cells, even without nuclei, undergo self-sustained cell cycle oscillations, as in real cells. Our droplet microfluidic system, capable of producing synchronous, self-sustained oscillations, provides a robust, quantitative platform to study the cell-cycle regulation at a high throughput (Figure S4).

The ability to create subcellular compartments, such as nucleus and cytosol, that can communicate with each other, a key characteristic of a living cell, is crucial for understanding cellular mechanisms, but has not been well developed. Here, using our droplet microfluidic technology, we further generated a novel artificial cell with a functional nucleus and quantitatively characterized its spatiotemporal heterogeneity for the first time. We supplemented the “simple” nucleus-free artificial cells with demembranated sperm chromatin to trigger self-assembly of nuclei surrounding the sperm DNA, GFP-tagged nuclear localization signal (GFP-NLS) to report nuclear formation, and an ATP energy regeneration system (Figure 4A,B, “complex” cell). These enable the creation of a complex cell with a nucleus that exhibits periodic morphology changes in time and space, that is, a nucleus forms during interphase with GFP-NLS translocating into the nucleus, forming a bright dot (Figure 4D, upper-row images), while the nuclear envelope breaks down in the mitotic phase, with NLS-GFP evenly distributed throughout the droplet (Figure 4D, bottom-row images; see also Movie S2). Previously, this could be a major challenge for an algorithm to automatically estimate the cell cycle period. In this study, we use the standard deviation of fluorescent intensity as a measurement for nucleus appearance and supervised learning to identify interphase and mitotic phase (Figure S7).

We found that the period of oscillations increased over time (Figure 4D); such a slowdown behavior was also observed in cells containing no nuclei (Figure 4C). The period prolongation could be explained by an energy depletion model in which the consumed ATP imposes a critical impact on the speed of the cell cycle.<sup>14</sup> Interestingly, the impact seems to be predominantly on the rising phase of oscillation or interphase, which extends at each cell cycle (Figure 4D red dots, Figure 4E), while the falling period or mitotic phase duration remains nearly constant (Figure 4D blue dots, Figure 4F). Using a cell cycle model (see the Supporting Information), we could recapitulate such differential behaviors of interphase and mitotic phase in response to energy reduction (Figure 4G). Consistent with previous studies of Cdk1-cyclin B1 clock in bulk solutions<sup>31</sup> and in mammalian cells,<sup>39</sup> our results reveal that cell cycle, which builds on a hysteretic switch by the Cdk1-Cdc25-Wee1 interlinked positive feedback loops and behaves as a relaxation oscillator, alternating between a long relaxation interphase period that is subject to environmental perturbations and a short impulsive mitotic period that is temporally insulated from variability.

Our first detectable cycle periods in nucleus and nucleus-free droplets last about 100–150 min (Figure 4D) and 50 min (Figure 4C), respectively, while the *in vivo* cycle period of *Xenopus* early embryos was found to be around 30–40 min.<sup>40</sup> Such a difference between *in vivo* and *in vitro* cycle periods has been observed earlier, but the explanation and mechanism have not been fully resolved yet<sup>41</sup> and could probably be attributed to differential energy levels, cytoplasm volume dilution, or temperature differences.

## CONCLUSIONS

In conclusion, we have developed a droplet microfluidic platform and analytical algorithm that enable generation, incubation, and detection of arrays of individual droplets. The unique and powerful combination of analytical abilities opens up exciting possibilities for studying cell-free systems, which oftentimes require microscale analyses at high throughput, high sensitivity, and high spatiotemporal resolution. Specifically, in this work, we reconstructed and quantified various cellular machineries in cell-free microdroplets (i.e., protein expression and degradation, cell-cycle oscillations, and nuclear morphology changes), utilizing three major types of (i.e., digital, analog, and morphological) measurements. Our results indicated that the droplet artificial cells enable efficient constitution and quantification of sophisticated spatiotemporal dynamics *in vitro*, manifesting its transforming potential in synthetic biology. It may eventually benefit the study of diseases and disorders at early stages of embryonic development that has been previously difficult to achieve without such a tool. In addition, the framework is easy to set up and straightforward to use, therefore, it can be adopted by any regular lab that has already been equipped with a conventional fluorescence microscope as a universal and low-cost solution to perform diversified types of droplet analysis; thus, it will ultimately be lowering the barrier of using droplet microfluidic technology for a broader range of applications, particularly in the fields of chemistry, physics, medicine, and biology.

## Supplementary Material

Refer to Web version on PubMed Central for supplementary material.

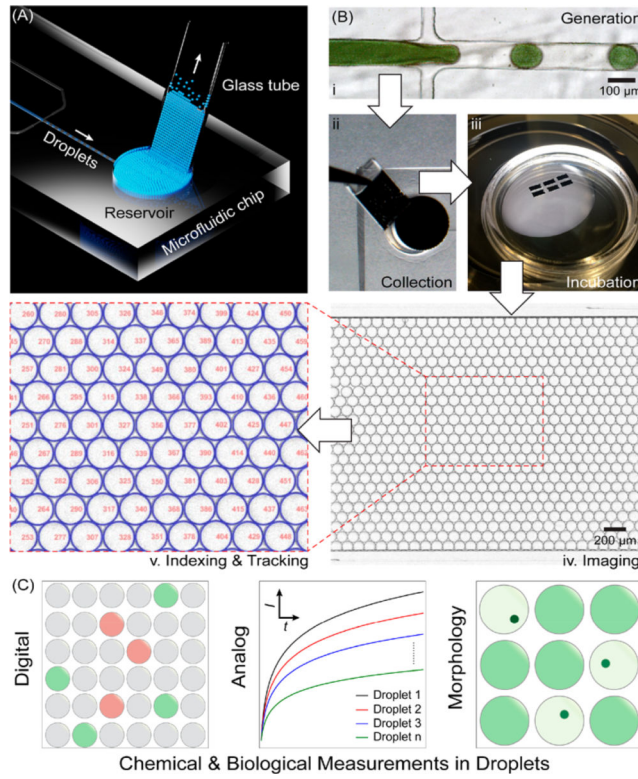
## ACKNOWLEDGMENTS

We thank Jeremy B. Chang and James E. Ferrell Jr. for providing GFP-NLS construct. We gratefully acknowledge the support from the National Science Foundation (Early CAREER Grant #1553031; MCB #1817909), the National Institutes of Health (MIRA #GM119688), and the Alfred P. Sloan Foundation.

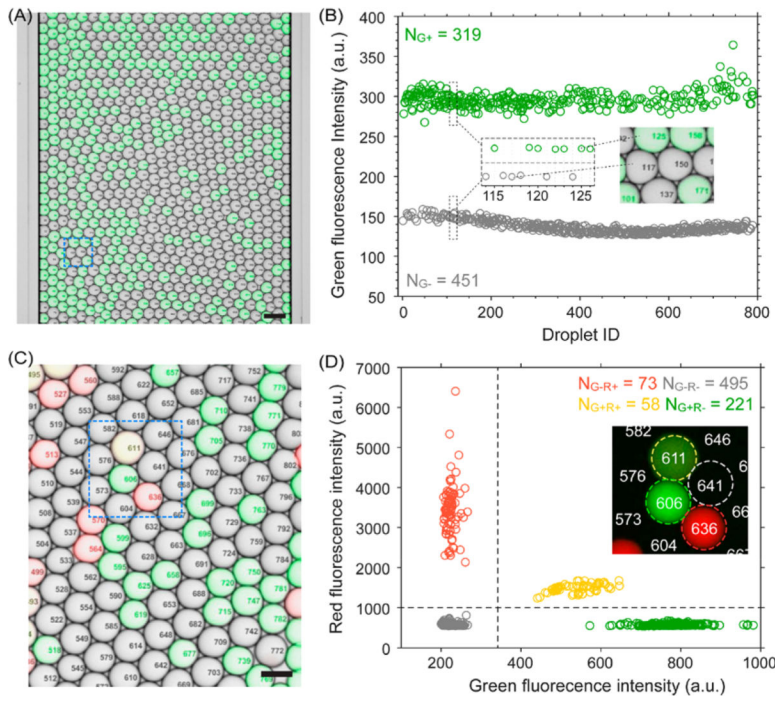
## REFERENCES

- (1). Smanski MJ; Zhou H; Claesen J; Shen B; Fischbach MA; Voigt CA *Nat. Rev. Microbiol.* 2016, 14, 135–149. [PubMed: 26876034]
- (2). Way JC; Collins JJ; Keasling JD; Silver PA *Cell* 2014, 157, 151–161. [PubMed: 24679533]
- (3). Buddingh BC; van Hest JC M. *Acc. Chem. Res.* 2017, 50, 769–777.
- (4). Lu Y. *Synth Syst. Biotechnol* 2017, 2, 23–27. [PubMed: 29062958]
- (5). Smith MT; Wilding KM; Hunt JM; Bennett AM; Bundy BC *FEBS Lett.* 2014, 588, 2755–2761. [PubMed: 24931378]
- (6). de Boer PA; Crossley RE; Rothfield LI *Cell* 1989, 56, 641–649. [PubMed: 2645057]
- (7). Scott MP; Carroll SB *Cell* 1987, 51, 689–698. [PubMed: 2890437]
- (8). Good MC; Vahey MD; Skandarajah A; Fletcher DA; Heald R. *Science* 2013, 342, 856–860. [PubMed: 24233724]
- (9). Hazel J; Krutkramelis K; Mooney P; Tomschik M; Gerow K; Oakey J; Gatlin JC *Science* 2013, 342, 853–856. [PubMed: 24233723]
- (10). Weitz M; Kim J; Kapsner K; Winfree E; Franco E; Simmel FC *Nat. Chem.* 2014, 6, 295–302. [PubMed: 24651195]
- (11). Damiati S; Mhanna R; Kodzius R; Ehmoser EK *Genes* 2018, 9, 144.
- (12). Gach PC; Iwai K; Kim PW; Hillson NJ; Singh AK *Lab Chip* 2017, 17, 3388–3400. [PubMed: 28820204]
- (13). Martino C; deMello AJ *Interface Focus* 2016, 6, 20160011.
- (14). Guan Y; Li Z; Wang S; Barnes PM; Liu X; Xu H; Jin M; Liu AP; Yang Q. *eLife* 2018, 7, na.
- (15). Mellouli S; Monterroso B; Vutukuri HR; Brinke E.t.; Chokkalingam V; Rivas G; Huck WTS. *Soft Matter* 2013, 9, 10493.
- (16). Sanchez T; Chen DT; DeCamp SJ; Heymann M; Dogic Z. *Nature* 2012, 491, 431–434. [PubMed: 23135402]
- (17). Sun M; Fang Q. *Lab Chip* 2010, 10, 2864–2868. [PubMed: 20714511]
- (18). Sun M; Khan ZS; Vanapalli SA *Lab Chip* 2012, 12, 5225–5230. [PubMed: 23114925]
- (19). Miller OJ; El Harrak A; Mangeat T; Baret JC; Frenz L; El Debs B; Mayot E; Samuels ML; Rooney EK; Dieu P; Galvan M; Link DR; Griffiths AD *Proc. Natl. Acad. Sci. U. S. A* 2012, 109, 378–383. [PubMed: 22203966]
- (20). Jakielia S; Kaminski TS; Cybulski O; Weibel DB; Garstecki P. *Angew. Chem., Int. Ed* 2013, 52, 8908–8911.
- (21). Kim GA; Ginga NJ; Takayama S. *Cell Mol. Gastroenterol Hepatol* 2018, 6, 123–131. [PubMed: 29928682]
- (22). Du W; Li L; Nichols KP; Ismagilov RF *Lab Chip* 2009, 9, 2286–2292. [PubMed: 19636458]
- (23). Bithi SS; Wang WS; Sun M; Blawdziewicz J; Vanapalli SA *Biomicrofluidics* 2014, 8, No. 034118.
- (24). Genot AJ; Baccouche A; Sieskind R; Aubert-Kato N; Bredeche N; Bartolo JF; Taly V; Fujii T; Rondelez Y. *Nat. Chem* 2016, 8, 760–767. [PubMed: 27442281]
- (25). Baccouche A; Okumura S; Sieskind R; Henry E; Aubert-Kato N; Bredeche N; Bartolo JF; Taly V; Rondelez Y; Fujii T; Genot AJ *Nat. Protoc* 2017, 12, 1912–1932. [PubMed: 28837132]
- (26). Huh S; Ker DF; Bise R; Chen M; Kanade T. *IEEE Trans Med. Imaging* 2011, 30, 586–596. [PubMed: 21356609]
- (27). Gibson DG; Young L; Chuang RY; Venter JC; Hutchison CA 3rd; Smith HO *Nat. Methods* 2009, 6, 343–345. [PubMed: 19363495]

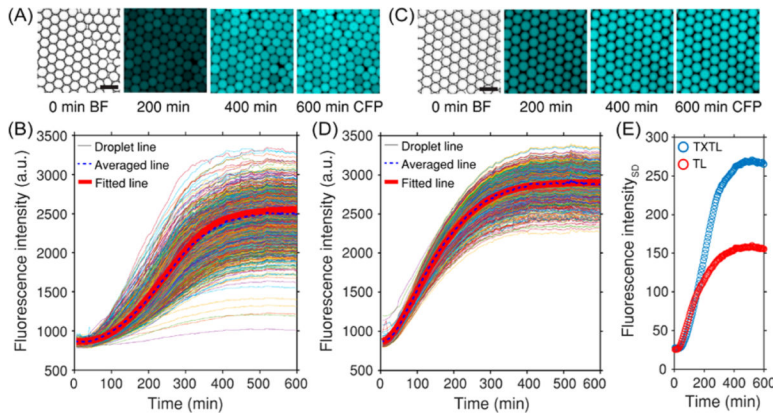
- (28). Murray AW *Methods Cell Biol.* 1991, 36, 581–605. [PubMed: 1839804]
- (29). Stogbauer T; Windhager L; Zimmer R; Radler JO *Integr Biol. (Camb)* 2012, 4, 494–501. [PubMed: 22481223]
- (30). Karzbrun E; Shin J; Bar-Ziv RH; Noireaux V. *Phys. Rev. Lett* 2011, 106, No. 048104.
- (31). Yang Q; Ferrell JE Jr. *Nat. Cell Biol* 2013, 15, 519–525. [PubMed: 23624406]
- (32). Hindson BJ; Ness KD; Masquelier DA; Belgrader P; Heredia NJ; Makarewicz AJ; Bright IJ; Lucero MY; Hiddessen AL; Legler TC; Kitano TK; Hodel MR; Petersen JF; Wyatt PW; Steenblock ER; Shah PH; Bousse LJ; Troup CB; Mellen JC; Wittmann DK; et al. *Anal. Chem* 2011, 83, 8604–8610. [PubMed: 22035192]
- (33). Basu AS *SLAS Technol.* 2017, 22, 369–386. [PubMed: 28448765]
- (34). Matthaei JH; Jones OW; Martin RG; Nirenberg MW *Proc. Natl. Acad. Sci. U. S. A* 1962, 48, 666–677. [PubMed: 14471390]
- (35). Noireaux V; Bar-Ziv R; Libchaber A. *Proc. Natl. Acad. Sci. U. S. A* 2003, 100, 12672–12677. [PubMed: 14559971]
- (36). Marshall R; Maxwell CS; Collins SP; Jacobsen T; Luo ML; Begemann MB; Gray BN; January E; Singer A; He Y; Beisel CL; Noireaux V. *Mol. Cell* 2018, 69, 146–157. [PubMed: 29304331]
- (37). Yamamoto T; Fujii T; Nojima T. *Lab Chip* 2002, 2, 197–202. [PubMed: 15100810]
- (38). Maerkli SJ; Quake SR *Science* 2007, 315, 233–237. [PubMed: 17218526]
- (39). Araujo AR; Gelens L; Sheriff RS; Santos SD *Mol. Cell* 2016, 64, 362–375. [PubMed: 27768873]
- (40). Anderson GA; Gelens L; Baker JC; Ferrell JE Jr. *Cell Rep.* 2017, 21, 37–46. [PubMed: 28978482]
- (41). Murray AW; Kirschner MW *Nature* 1989, 339, 275–280. [PubMed: 2566917]

**Figure 1.**

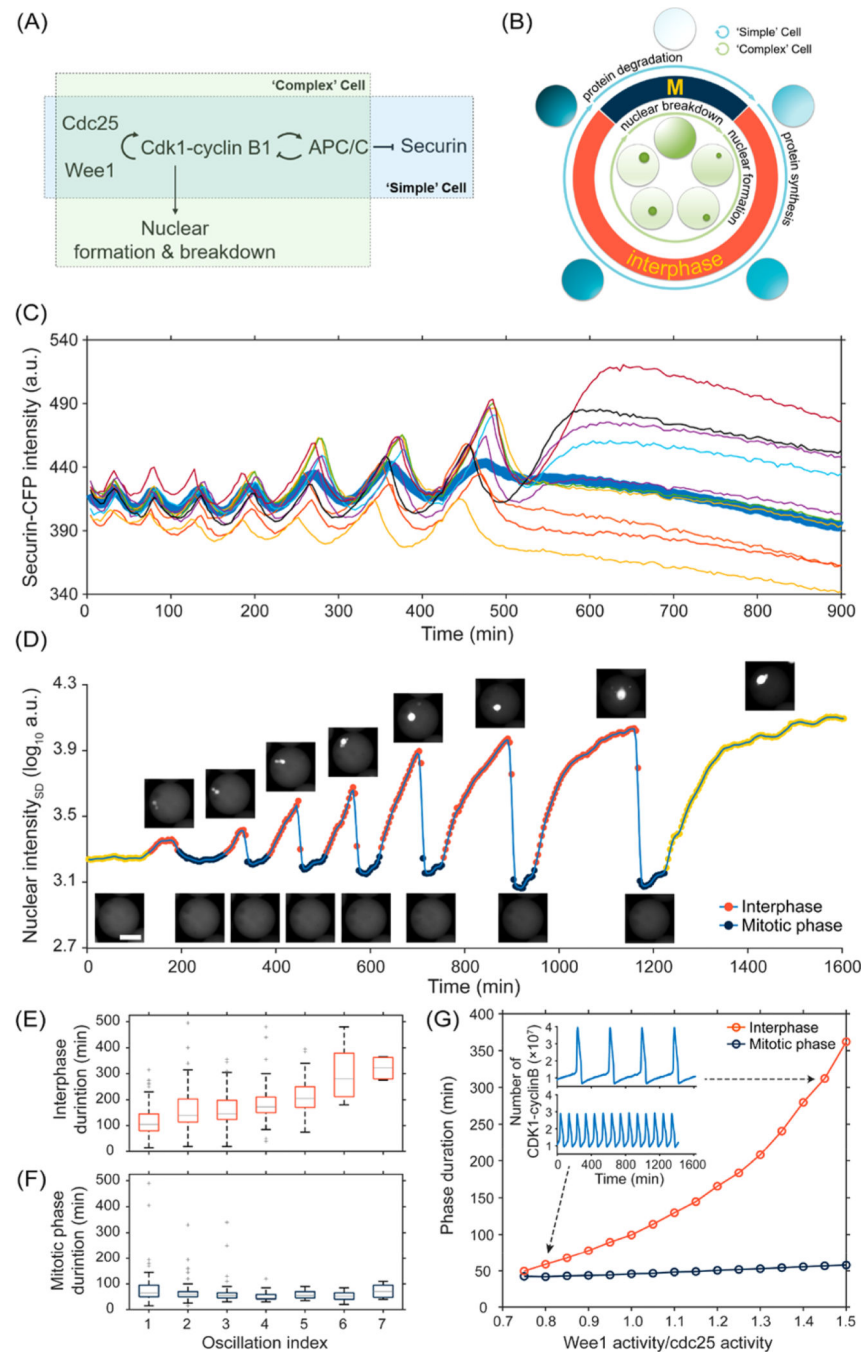
Droplet microfluidic platform. (A) Schematic diagram showing droplet generation and loading into a glass tube: a reservoir opened at the end of a flow-focusing device with a diameter of 3 mm; the tube width is 2.1 mm. The arrows indicate the flow direction of droplets. (B) Droplet microfluidic workflow: droplet (i) generation; (ii) collection; (iii) incubation; (iv) imaging (e.g., a phase-contrast image showing the collected water droplets in a glass tube); and (v) bright-field indexing and tracking. (C) Representative applications of the platform for droplet analysis in three typical types of chemical and biological assays.

**Figure 2.**

Droplet detection, tracking, and analysis. (A) A composite of bright-field and fluorescent channels showing a mixture of droplets of water (gray) and droplets of fluorescein sodium (green) in a glass tube. Scale bar: 200  $\mu\text{m}$ . (B) Fluorescence intensities of the droplets shown in (A). A total of  $N_{\text{G}+} = 319$  fluorescent droplets (green circle) and  $N_{\text{G}-} = 451$  water droplets (gray circle) are detected and indexed with unique IDs. The inset shows enlarged views of the droplets outlined in (A), indexed from numbers 114 to 126. (C) A composite of bright-field and fluorescent images showing four droplet species detected and distinguished by their fluorescent signals in a portion of a tube: green (fluorescein sodium); red (NHS-Rhodamine); yellow (1:1 mixture of green and red); gray (water). Scale bar: 100  $\mu\text{m}$ . (D) Fluorescence intensity analysis of all the droplets collected in the tube of (C). The inset shows a fluorescent and enlarged view of the droplets outlined in (C), where color-dashed circles indicate the selected examples from four droplet species: green ( $\text{G} + \text{R}-$ ), red ( $\text{G}- \text{R}+$ ), yellow ( $\text{G} + \text{R}+$ ), and gray ( $\text{G} - \text{R}-$ ).  $N$  represents the total number of the detected droplets in each corresponding species.

**Figure 3.**

Synthesis of securin-CFP in artificial droplet cells via in vitro (A, B) transcription–translation (TXTL) and (C, D) translation (TL). (A, C) Selected time-lapse images showing the increasing brightness of CFP signal in droplets over a course of 600 min in both TXTL and TL assays. The fluorescence intensities of droplets at time zero are invisible, and bright-field images are shown instead. (B, D) Solid colored lines showing CFP fluorescent intensities increased with protein synthesis and reached plateaus in individual droplets in TXTL assays ( $n = 1639$ ) and TL assays ( $n = 1604$ ), respectively. The blue dashed lines showing the medians and the thick red lines showing the model fit results. (E) Standard deviations of the fluorescence intensities in (B) and (D), indicating the variation difference in the TXTL and TL assays. Images and data were collected every 5 min at room temperature. Scale bars:  $100 \mu\text{m}$ .

**Figure 4.**

Reconstruction of cell-cycle oscillators in microdroplets. (A) Schemes of biocircuits of “simple” and “complex” cells. (B) Diagram of cell-cycle oscillator shows alternating interphase (red segment) and mitotic phase (blue segment) in “simple” and “complex” cells. (C) Synthesis and degradation of securing-CFP in “simple” cell cycles. A total of 10 selected traces with an average (ticked blue line) from 376 droplet oscillators (full traces shown in Figure S6). (D) Cell cycle oscillations in “complex” cells containing *Xenopus* extract and sperm DNA labeled with NLS-GFP. Images above and beneath the curve show a

representative droplet oscillating between interphase (red dots) and mitotic phase (blue dots). Yellow dots indicate pre-and postoscillation periods. Scale bar: 50  $\mu\text{m}$ . Periods of interphase (E) and mitotic phase (F) vs cycling number. (G) Theoretical modeling of the periods of oscillations at the interphase and mitotic phase, consistent with our experimental observations. Images were captured every 5 and 4 min for the experiments in (C) and (D), respectively.